J. Fluid Mech. (2013), *vol.* 724, *pp.* 581–606. © Cambridge University Press 2013
doi:10.1017/jfm.2013.130

Direct numerical simulation of top-down and bottom-up diffusion in the convective boundary layer

Scott B. Waggy[1], Sedat Biringen[1,†] and Peter P. Sullivan[2]

[1]Department of Aerospace Engineering Sciences, University of Colorado, Boulder, CO 80309, USA
[2]National Center for Atmospheric Research, Boulder, CO 80307, USA

(Received 14 April 2012; revised 1 February 2013; accepted 26 February 2013;
first published online 30 April 2013)

A direct numerical simulation (DNS) of an unstably stratified convective boundary layer with system rotation was performed to study top-down and bottom-up diffusion processes. In order to better understand near-wall dynamics associated with scalar diffusion in the absence of surface roughness, direct simulation is utilized to numerically integrate the governing equations that model the atmospheric boundary layer. The ratio of the inversion height to Obukhov length scale, $z_i/L = -49.1$, indicates moderately strong heating for the case studied. Two passive scalars were initialized in the flow field: the first with a zero gradient at the wall (q_t, top-down diffusion), and the second with a non-zero wall gradient and a close-to-zero gradient at the height of the temperature inversion (q_b, bottom-up diffusion). Scalar flux, variance and covariance profiles show good agreement between the DNS and rough-wall large-eddy simulation (LES). The top-down gradient function displays a slight increase in amplitude, indicating reduced mixing efficiency for the smooth-wall, low-Reynolds-number convective boundary layer. For the bottom-up process, the gradient matches other rough-wall simulations. The only notable difference between the smooth-wall DNS data and other rough-wall simulations is an increase in the gradient function near the wall. This indicates that the bottom-up gradient functions for a rough wall and a smooth wall are nearly identical except as the viscous sublayer is approached. Finally, a new empirical model for the scalar variance of a bottom-up scalar is proposed: here, a single function replaces two piecewise relationships to accurately capture the DNS results up to the viscous sublayer. The scalar covariance between top-down and bottom-up processes agrees with rough-wall and tree-canopy LES results; this indicates that the scalar covariance is independent of both Reynolds number and surface friction.

Key words: atmospheric flows, turbulence simulation, turbulent convection

1. Introduction

In the unstably stratified atmospheric boundary layer (ABL), mean velocity and potential temperature are well mixed below the capping inversion. To account for non-zero gradients in the mixed layer for specific humidity, Wyngaard & Brost (1984)

† Email address for correspondence: biringen@colorado.edu

https://doi.org/10.1017/jfm.2013.130 Published online by Cambridge University Press

proposed the concept of top-down and bottom-up diffusion. Given a scalar concentration c, Wyngaard & Brost describe the total scalar flux as a linear combination of the surface flux (subscript b) and entrainment-zone flux (subscript t):

$$\overline{w'c'} = \overline{w'c'}_b + \overline{w'c'}_t. \tag{1.1}$$

Top-down diffusion characterizes entrainment processes near the potential temperature inversion that occurs in the atmospheric boundary layer. A scalar is under the influence of top-down diffusion alone when the scalar flux is zero at the wall and is at a maximum at a height h_1. Conversely, bottom-up diffusion has a non-zero wall flux but zero flux at h_1. These two processes are clearly shown in figures 4 and 5 of Wyngaard & Brost (1984).

Such a decomposition allows the two separate processes to be modelled individually. By means of large-eddy simulation (LES), Wyngaard & Brost (1984) parametrized the eddy diffusivity for both top-down and bottom-up passive scalars by treating the processes as symmetric. Their results show good agreement between LES and their proposed closure approximation. Moeng & Wyngaard (1984) built upon this analysis by constructing functions to parametrize scalar covariances and compute the flux budgets for both top-down and bottom-up scalars. The two production terms (buoyant and scalar gradient) in the flux budgets are found to behave differently for the bottom-up and top-down processes. Consequently, a model of the flux that does not account for the different behaviours will probably perform poorly when both processes are significant.

The gradient functions g_t and g_b for a scalar c are generalized as

$$\frac{\partial c_t}{\partial z} = -\frac{\overline{w'c'}_1}{w_* z_i} g_t \tag{1.2}$$

and

$$\frac{\partial c_b}{\partial z} = -\frac{\overline{w'c'}_0}{w_* z_i} g_b. \tag{1.3}$$

If the gradient functions above are known, the gradient of an arbitrary scalar ($\partial c/\partial z$) can be approximated by a linear combination of g_t and g_b. Wyngaard & Brost (1984) and Moeng & Wyngaard (1984) propose models of these gradient functions for a rough-wall convective boundary layer. Piper *et al.* (1995) performed a water-tank experiment of top-down and bottom-up convection using dye and temperature measurements. Their results demonstrated close agreement with the gradient functions proposed by Wyngaard & Brost (1984) and Moeng & Wyngaard (1984). Patton, Sullivan & Davis (2003) and Wang *et al.* (2007) proposed revisions to the gradient functions given by Wyngaard & Brost (1984) for a convective boundary layer over a forested site where the canopy acts to increase surface roughness.

The purpose of this work is to simulate passive scalars as bottom-up and top-down processes over a smooth surface while resolving flow features through the viscous sublayer and down to the wall via direct numerical simulation (DNS). This allows a fundamental study of the two diffusion processes in the absence of a rough wall and avoids assumptions concerning near-wall temperature and scalar fluxes. Furthermore, Sullivan & Patton (2011) demonstrated that increasing mesh resolution leads to an increase in the magnitude of various third-order moments (see also Moeng & Wyngaard 1988, 1989). Directly simulating the convective boundary layer will assist in illustrating the effects that small scales may have on the top-down and bottom-up

https://doi.org/10.1017/jfm.2013.130 Published online by Cambridge University Press

diffusion processes. Comparison between DNS results and previous LES simulations also provides insight into the effect of surface roughness on scalar flux. Adrian, Ferreira & Boberg (1986) noted similarity in the large scales of laboratory-generated thermal convection when $Re_c > 500$. Although a significant difference in Reynolds number exists between atmospheric dynamics and the present simulation, it is expected that major differences will be a result of the surface roughness or the strength of unstable buoyant forcing, and not, necessarily, caused only by the low Reynolds number of the simulation. The DNS presented is well above the limit ($Re_c > 4000$; see § 3) set by Adrian *et al.* (1986), so large-scale features are expected to be similar to flows with higher Reynolds numbers. Furthermore, Willis & Deardorff (1974) and Deardorff & Willis (1985) claim Reynolds number independence for their water-tank experiments of the convective boundary layer when Re_c is approximately 6500 and 1500, respectively. Additional support for the assumption that results from the DNS display Reynolds number similarity is given by Moeng & Wyngaard (1988), Wyngaard (2010) and Sullivan & Patton (2011).

2. Simulation specifications

To study top-down and bottom-up processes, a DNS of the incompressible Navier–Stokes equations and energy equation with rotation and buoyancy is performed. The following sections discuss the governing equations (§ 2.1), numerical solution procedure (§ 2.2) and initial/boundary conditions (§ 2.3).

2.1. *Governing equations*

The Ekman layer with a heated surface and capped inversion is used to approximate the unstably stratified ABL. The governing equations, in conservative form and with the Boussinesq approximation for the buoyancy, are given by

$$\frac{\partial u_i}{\partial x_i} = 0, \tag{2.1a}$$

$$\frac{\partial u_i}{\partial t} + \frac{\partial u_i u_j}{\partial x_j} + \frac{1}{Ro} u_j \varepsilon_{ji3} = -\frac{\partial P}{\partial x_i} + \frac{1}{Re}\nabla^2 u_i + \theta \delta_{i3}, \tag{2.1b}$$

$$\frac{\partial \theta}{\partial t} + \frac{\partial u_j \theta}{\partial x_j} = \frac{1}{RePr}\nabla^2 \theta, \tag{2.1c}$$

$$\frac{\partial q}{\partial t} + \frac{\partial u_j q}{\partial x_j} = \frac{1}{ReSc}\nabla^2 q. \tag{2.1d}$$

Here, u_i corresponds to the (u_1, u_2, u_3) or (u, v, w) velocity components in the (x_1, x_2, x_3) or (x, y, z) directions, where x_3 (z) is the wall-normal direction. The Reynolds number $Re = U_g \delta_E / \nu$ is defined in terms of the geostrophic velocity (U_g), the Ekman depth $(\delta_E = \sqrt{\nu/\Omega})$ and the kinematic viscosity (ν). System rotation is aligned with the wall-normal direction at a rate of Ω; its effects are included via a Rossby number $Ro = U_g / 2\Omega\delta_E$. The dimensionless potential temperature θ is given by

$$\theta = \frac{g\delta_E}{U_g^2}\left(\frac{T - T_0}{T_0}\right), \tag{2.2}$$

where g is the gravitational constant and T_0 is a reference temperature. Also, P is the pressure normalized by the density and q is the concentration of a passive scalar. The Prandtl number $Pr = \nu/\kappa$ is the ratio of viscous to thermal diffusion, and the Schmidt number $Sc = \nu/D$ is the ratio of viscous to molecular diffusion for the given scalar.

https://doi.org/10.1017/jfm.2013.130 Published online by Cambridge University Press

In (2.1*b*) we have adopted the Boussinesq approximation to introduce buoyant forcing into the vertical momentum equation:

$$-\rho g\hat{k} = -\rho_0 g\left(1 - \frac{T - T_0}{T_0}\right)\hat{k}. \tag{2.3}$$

Hydrostatic pressure ($-\rho_0 g\hat{k}$) is included in the mean pressure gradient $\partial P/\partial x_i$ along with the centrifugal component of system rotation ($\Omega^2\boldsymbol{R}$, where $\boldsymbol{R}$ is the radius from the centre of the axis of rotation to the fluid element). For this work, we assume the geostrophic approximation, i.e. Coriolis forces and the pressure gradient are in balance. Consequently, the mean pressure gradient is defined such that the geostrophic velocity U_g aligns with the x axis:

$$-\frac{\partial \overline{P}}{\partial x_i} = -\frac{2}{Re}\delta_{i2}. \tag{2.4}$$

The overbar is used to indicate the fact that (2.4) denotes a mean pressure gradient; pressure fluctuations are solved for in the numerical scheme.

2.2. *Numerical solution procedure*

The governing equations given by (2.1) were solved using a semi-implicit fractional-step method based on the implicit Crank–Nicolson and the explicit Adams–Bashforth methods (see Waggy *et al.* 2012). Accordingly, vertical diffusion terms are advanced implicitly; all remaining terms (horizontal diffusion, Coriolis, advection) are explicitly solved for based on the previous two time realizations. The time advancement scheme for the velocity is as follows:

$$\left(1 - \frac{\Delta t}{2Re}\frac{\partial^2}{\partial x_3^2}\right)\hat{u}_i = u_i^n + \Delta t\left(\frac{1}{2}M_i^n + \frac{3}{2}L_i^n - \frac{1}{2}L_i^{n-1}\right) + O(\Delta t^2), \tag{2.5}$$

where

$$M_i^n = \frac{1}{Re}\frac{\partial^2 u_i^n}{\partial x_3^2} \tag{2.6}$$

and

$$L_i^n = -\frac{\partial u_i^n u_j^n}{\partial x_j} - \frac{1}{Ro}u_j^n\varepsilon_{ji3} - \frac{\partial P}{\partial x_i} + \frac{1}{Re}\left(\frac{\partial^2 u_i^n}{\partial x_1^2} + \frac{\partial^2 u_i^n}{\partial x_2^2}\right) + \theta^n\delta_{i3}. \tag{2.7}$$

In the above expressions, u_i^n refers to the velocity component in the x_i direction at the nth time step. The hat denotes a predicted quantity at the fractional step. A correction from the predicted velocity to the velocity at the $(n+1)$th iteration is accomplished by defining a pseudo-pressure ϕ such that

$$\frac{u_i^{n+1} - \hat{u}_i}{\Delta t} = -\frac{\partial \phi}{\partial x_i}. \tag{2.8}$$

This allows a zero divergence to be enforced on u_i^{n+1}:

$$\frac{1}{\Delta t}\left(\frac{\partial u_i^{n+1}}{\partial x_i} - \frac{\partial \hat{u}_i}{\partial x_i}\right) = -\frac{\partial^2 \phi}{\partial x_i \partial x_i}. \tag{2.9}$$

https://doi.org/10.1017/jfm.2013.130 Published online by Cambridge University Press

Re	1000
Pr	1
Sc	1
Ri_0	-1
L_x/z_i	6.04
L_y/z_i	6.04
$N_x = N_y$	512
L_z/z_i	6.71
N_z	256
Δz^+_{min}	0.931

TABLE 1. Simulation parameters in the DNS: Reynolds number $Re = U_g\delta_E/\nu$, Prandtl number $Pr = \nu/\kappa$, Schmidt number $Sc = \nu/D$, surface Richardson number $Ri_0 = [g\delta_E^2/(T_0U_g^2)]\,\partial T/\partial\tilde{z}|_{\tilde{z}=0}$, domain size (L_x, L_y, L_z), number of mesh points (N_x, N_y, N_z), and minimum vertical mesh spacing (Δz^+_{min}). Note that z_i is the height of the temperature inversion.

Since $\partial u_i^{n+1}/\partial x_i = 0$, a linear system of equations for ϕ can be solved since $\hat{u}_i$ is known:

$$-\Delta t\frac{\partial^2\phi}{\partial x_i\partial x_i} = \frac{\partial\hat{u}_i}{\partial x_i}. \tag{2.10}$$

Rearranging, (2.8) yields the velocity at the new time step.

$$u_i^{n+1} = \hat{u}_i - \Delta t\frac{\partial\phi}{\partial x_i}. \tag{2.11}$$

Integration of the equations for potential temperature and passive scalars follows the same procedure as above, except that no pressure correction is required. As evident in (2.7), the potential temperature θ is lagged by one time step.

Spatial differences are obtained by using fourth-order-accurate, centred finite differences in all three coordinate directions. A staggered and stretched mesh is employed in the vertical direction to accommodate sharp gradients close to the lower boundary. Interpolation between the wall-coincident mesh and the staggered grid is accomplished via Lagrangian polynomials. Further discussion of the numerical techniques used to solve (2.1) is given by Waggy *et al.* (2012). The values of the parameters described above for the current test case are provided in table 1.

Figure 1 shows the largest $(\mathscr{L} = k^{3/2}/\varepsilon)$ and smallest $(\eta = (\nu^3/\varepsilon)^{1/4})$ length scales of turbulence with respect to the horizontal computational mesh. Additionally, the Taylor micro-scale λ (see § 4) is shown. In order to prevent the occurrence of grid-to-grid oscillations, an artificial dissipation term (Anderson, Tannehill & Pletcher 1984) was added,

$$L^n_{u_i} = \cdots + \beta\Delta x_j^4\frac{\partial^4 u_i^n}{\partial x_j^4}, \tag{2.12}$$

where β controls the strength of the dissipation; for the present simulations $\beta = 0.8$. The magnitude of the artificial dissipation term remained about two orders of magnitude smaller than viscous dissipation throughout the computation. Consequently, its effect on the present results was negligible.

Validation of the DNS code was accomplished by comparing numerical solutions of instability wave propagation in plane channel flow with linear stability theory using

https://doi.org/10.1017/jfm.2013.130 Published online by Cambridge University Press

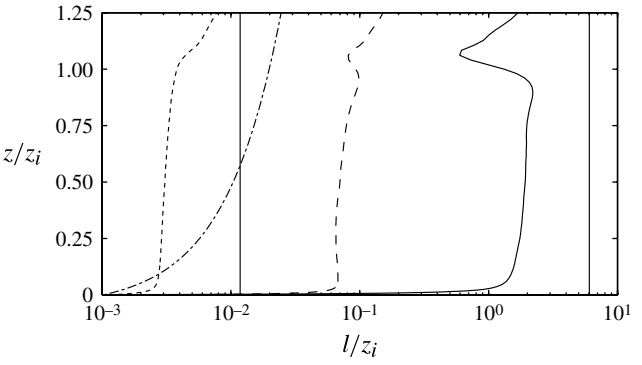


FIGURE 1. Computational resolution: solid line, largest turbulent scale, $\mathscr{L} = k^{3/2}/\varepsilon$; long dashed line, Taylor micro-scale, $\lambda = \sqrt{15\nu u'/\varepsilon}$; short dashed line, Kolmogorov scale, $\eta = (\nu^3/\varepsilon)^{1/4}$; dot-dashed line, vertical mesh resolution, Δz; vertical lines, maximum (L_x, L_y) and minimum $(L_x/N_x, L_y/N_y)$ horizontal scales.

the Orr–Sommerfeld equation (see Waggy *et al.* 2012) at two different Reynolds numbers. Results from the study indicated that the growth of the disturbance amplitudes deviated from the linear theory by less than 1 % over the integration time $0 \leqslant t \leqslant 10$. Furthermore, neutral Ekman layer studies performed using the same numerical procedure (Marlatt, Waggy & Biringen 2010; Waggy, Marlatt & Biringen 2011; Marlatt, Waggy & Biringen 2012) compare very favourably with results from the literature (Coleman, Ferziger & Spalart 1990; Miyashita, Iwamoto & Kawamura 2006; Spalart, Coleman & Johnstone 2008).

2.3. *Boundary and initial conditions*

A no-slip boundary condition is enforced on the wall for all velocity components: $u = v = w = 0$ at $z = 0$. At the top of the domain, a stress-free and a zero-flux condition are enforced: $\partial u/\partial z = \partial v/\partial z = w = 0$ at $z = z_{max}$.

The initial temperature profile shown in figure 2 was imposed directly onto a fully developed neutrally stratified turbulent Ekman layer simulation (for details, see Marlatt *et al.* 2012) in the same manner as used by Coleman & Ferziger (1994):

$$\theta = \frac{\gamma\pi^{1/2}}{2} Ri_0 \left[\operatorname{erf}\left(\frac{z}{\gamma}\right) + \operatorname{erf}\left(\frac{b_* - z}{\gamma}\right)\right], \quad 0 \leqslant z \leqslant b_*, \tag{2.13a}$$

$$\theta = -\frac{\gamma\pi^{1/2}}{2} Ri_0 \left[\operatorname{erf}\left(\frac{z - b_*}{\gamma}\right)\right] + \theta_{z=0}, \quad z \geqslant b_*, \tag{2.13b}$$

where $\gamma = a_* (-\ln 0.01)^{-1/2}$ and all variables have been non-dimensionalized by the Ekman depth δ_E (since the temperature field is directly imposed onto a neutrally stratified turbulent Ekman layer data set). The parameters a_* and b_* are used to control the depth of the temperature inversion (see Coleman & Ferziger 1994) and are set to $a_* = 4$ and $b_* = 10$. The surface Richardson number Ri_0 controls the initial strength of unstable stratification and is defined by

$$Ri_0 = \frac{g\delta_E^2}{T_0 U_g^2} \left.\frac{\partial T}{\partial \tilde{z}}\right|_{\tilde{z}=0}, \tag{2.14}$$

https://doi.org/10.1017/jfm.2013.130 Published online by Cambridge University Press

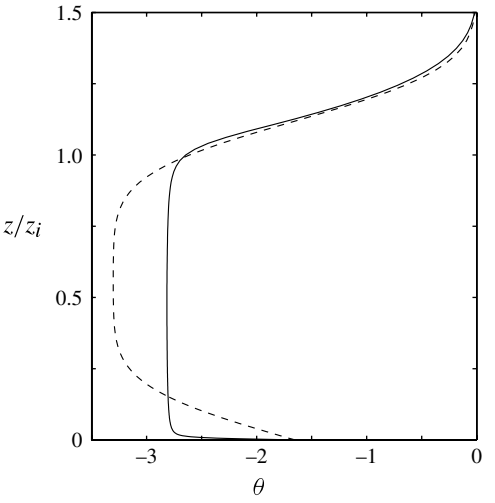


FIGURE 2. Mean potential temperature profile: solid line, time-averaged θ; dashed line, initial condition.

where $\tilde{z}$ is the dimensional wall-normal coordinate. In terms of dimensionless variables, this is simply written as

$$Ri_0 = \left.\frac{\partial\theta}{\partial z}\right|_{z=0}. \tag{2.15}$$

The flow was initialized with $Ri_0 = -1$ and allowed to evolve naturally with time. Both the lower and upper boundaries are set to a constant temperature. To ensure that no internal waves are reflected off the top boundary by the numerical scheme (Coleman & Ferziger 1994), the temperature gradient $\partial\theta/\partial z \to 0$ as $z \to \infty$. Thus, the curvature in the temperature profile at the top of the domain is a consequence of the upper boundary condition. The shape of the capping inversion for $z > z_i$ is reminiscent of the convective tank experiments of Deardorff & Willis (1985) and Piper *et al.* (1995). As the flow evolves with time, a mixed layer quickly develops and the near-wall temperature gradient grows. Over the time-averaging period used for this study (see § 3), the mean surface Richardson number decreases to $Ri_0 = -14.02$, indicating vigorous surface heating.

Once the unstably stratified simulation reached a quasi-steady state based on the convergence of Ri_0, two scalars were initialized in the domain with small-amplitude random fluctuations. The first passive scalar q_b was initialized with a constant value through most of the boundary layer and with a steep gradient near the wall. A constant scalar value ($q_b = 1$) condition was imposed at the wall with $\partial q_b/\partial z = 0$ at z_{max}. The top-down scalar q_t was initialized using a step function and allowed to evolve with a zero gradient condition at the wall. The height of the initial step function for q_t was chosen to align with the temperature inversion height (though z_i grows with time). With the newly introduced passive scalars q_b and q_t, the field was advanced forwards in time until a quasi-steady state was reached. Field variables were then averaged using 50 data realizations. The mean profiles of q_b and q_t are shown with their corresponding initial distribution in figure 3(*a*) and (*b*), respectively. The near-wall resolution allows the steep gradient in the initial distribution of q_b to be

https://doi.org/10.1017/jfm.2013.130 Published online by Cambridge University Press

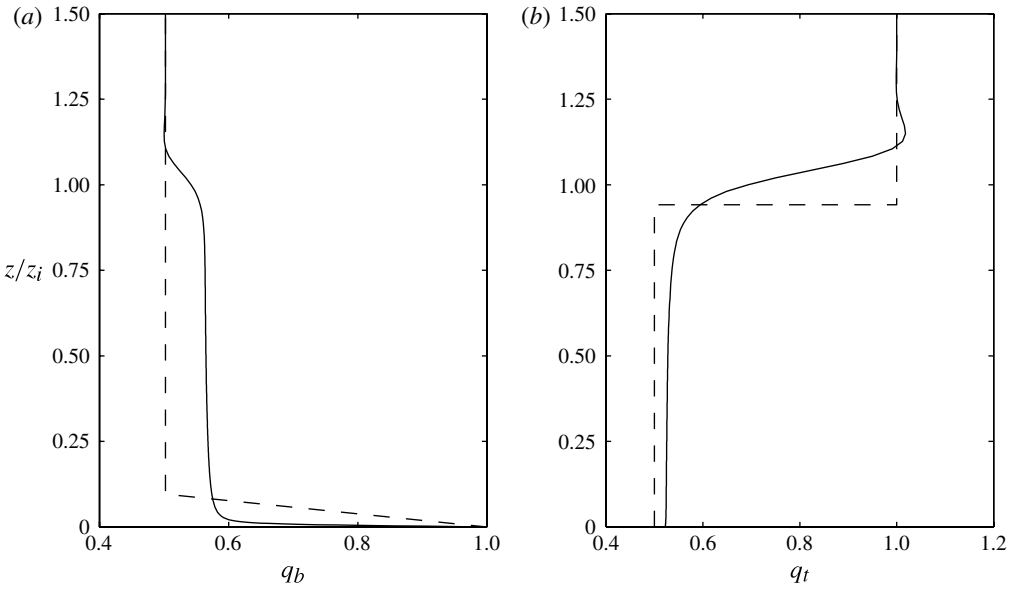


FIGURE 3. Mean scalar profiles for (*a*) q_b and (*b*) q_t. Dashed lines indicate initial conditions, while solid lines show time-averaged profiles.

well captured. For q_t, the step-function initial distribution occurred over a single mesh point. Although this distribution was quickly smoothed, the small region where $q_t > 1$ is a consequence of the discontinuous initial condition. Given the height at which this phenomenon occurs, it was found to have negligible impact on the region of interest in this study ($0 \leqslant z \leqslant z_i$).

3. Convective scales

Characteristic scales for the problems are taken to be the inversion height z_i and convective velocity (Deardorff 1972)

$$w_* = \left(\frac{gQ_{\theta,0}z_i}{T_0}\right)^{1/3}, \tag{3.1}$$

where $Q_{\theta,0}$ is the surface heat flux. At the wall, $\overline{w'\theta'} = 0$ due to the no-slip wall boundary condition, $w = 0$. Thus, the total heat flux at $z = 0$ is given by the viscous flux only:

$$Q_{\theta,0} = -\frac{k}{c_p\rho}\frac{\partial T}{\partial \tilde{z}} \tag{3.2}$$

or

$$\frac{Q_{\theta,0}}{U_g T_0} = -\frac{1}{RePr}\left.\frac{\partial \theta}{\partial z}\right|_{z_0}. \tag{3.3}$$

Combining (3.1) and (3.3), the convective velocity is written in dimensionless form as

$$\frac{w_*}{U_g} = \left[-\left(\frac{z_i}{\delta_E}\right)\left(\frac{1}{RePr}\right)\left(\frac{\partial \theta}{\partial z}\right)_{z=0}\right]^{1/3}. \tag{3.4}$$

https://doi.org/10.1017/jfm.2013.130 Published online by Cambridge University Press

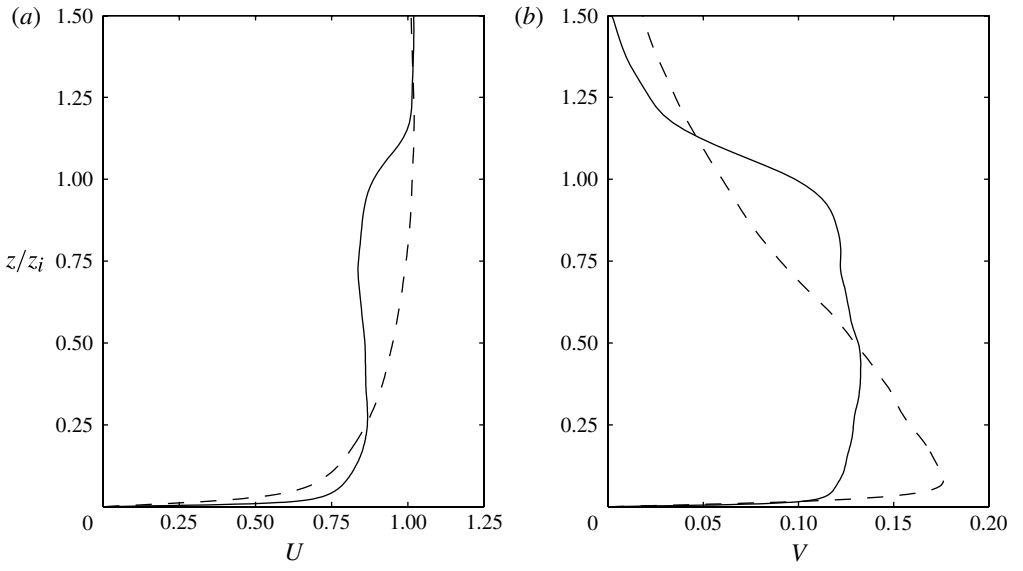


FIGURE 4. Mean velocity profiles in (*a*) streamwise and (*b*) spanwise directions. Dashed lines indicate neutrally stratified turbulent Ekman layer, and solid lines show unstably stratified simulation.

For this work, z_i is defined as the height at which the turbulent flux $\overline{w'\theta'}$ is minimum (Sullivan *et al.* 1998). Given characteristic scales w_* and z_i, the large-eddy turnover time is calculated as $\mathscr{T} = z_i/w_*$ (Deardorff 1972). The data for this work were averaged over a sampling window of $t/\mathscr{T} \approx 1.4$, i.e. an entire large-eddy turnover time was captured (note that the averaging window begins after the field has evolved for $> 6\mathscr{T}$ after initializing the temperature field). The interval $t/\mathscr{T} \approx 1.4$ corresponds to an averaging window of $tf \approx 0.05$ in terms of the Coriolis parameter.

The strength of the surface heating is determined by the ratio of the inversion height to the Obukhov length scale, z_i/L, with L given by (Obukhov 1971)

$$L = -\frac{u_*^3 T_0}{g\kappa Q_{\theta,0}}, \tag{3.5}$$

where u_* is the friction velocity and $\kappa = 0.41$ is the von Kármán constant. A dimensionless form of (3.5) is given by

$$\frac{L}{\delta_E} = \left(\frac{u_*}{U_g}\right)^3 \left(\frac{RePr}{\kappa}\right) \left(\frac{\partial\theta}{\partial z}\right)^{-1}_{z=0}. \tag{3.6}$$

For the present simulation, $z_i/L = -49.1$, which indicates moderately strong heating in the same regime as Wyngaard & Brost (1984), $z_i/L = -64$, Moeng & Wyngaard (1984), $z_i/L = -10$, and Wang *et al.* (2007), $z_i/L = -17.9$. LeMone (1973) notes the existence of roll cells only under mild heating, when $0 < -z_i/L < 10$. As will be shown in § 4, the mixed layer of the DNS is dominated by convective cells.

Owing to surface heating, the mean velocity profiles change quite dramatically. As shown in figure 4, the surface heating causes a well-mixed region to develop between $0 < z < z_i$ with nearly vertically uniform streamwise and spanwise velocities.

https://doi.org/10.1017/jfm.2013.130 Published online by Cambridge University Press

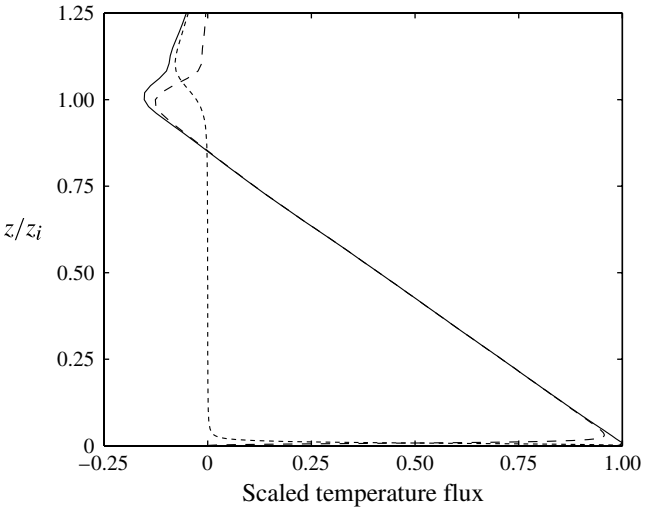


FIGURE 5. Vertical temperature flux: solid line, total temperature flux; long dashed line, turbulent flux; short dashed line, viscous flux. All terms have been normalized by $Q_{\theta,0}$ (3.3).

The presence of stable stratification causes a jump in the streamwise velocity profile across z_i.

The total temperature flux is composed of both turbulent and viscous flux components:

$$Q_\theta = \overline{w'\theta'} - \frac{1}{RePr}\frac{\partial\theta}{\partial z}. \tag{3.7}$$

The contributions of each term are shown in figure 5. Note that viscous effects only are prevalent in the very near-wall region and when $z \geqslant z_i$. Furthermore, it is clear that the heat flux maintains a linear shape for $0 \leqslant z/z_i \leqslant 1$. The minimum heat flux at $z = z_i$, which gives an indication of the strength of top-down diffusion to bottom-up diffusion and also entrainment, has a value of $Q_\theta/Q_{\theta,0} = -0.153$. Sorbjan (2004) simulated the unstable ABL under various conditions with $-4.17 \leqslant z_i/L \leqslant -1.95$ using LES. In Sorbjan's LES, the ratio between the total heat flux at the top and bottom of the mixed layer varied between approximately -0.17 and -0.3. Our results indicate slightly less entrainment influences at the top of the mixed layer relative to the bottom when stronger stratification is present (Jonker *et al.* 2010).

In the same fashion as (3.2), a surface flux parameter is defined for the bottom-up scalar q_b:

$$\frac{Q_{q_b,0}}{U_g} = -\frac{1}{ReSc}\frac{\partial q_b}{\partial z}\bigg|_{z_0}. \tag{3.8}$$

Note that q_b is a dimensionless scalar concentration, so $Q_{q_b,0}/U_g$ is likewise a dimensionless flux. The total, turbulent and viscous fluxes for q_b are shown in figure 6(*a*). The near-wall region is once again dominated by viscous flux, as the no-slip condition enforces zero turbulent flux. However, for $z/z_i > 0.04$, the viscous term is less than 1 % of $Q_{q_b,0}$ where $\overline{w'\theta'}$ is the primary transport mechanism. At the inversion, $Q_{q_b,0}/U_g = 0.06$, indicating very weak scalar flux.

https://doi.org/10.1017/jfm.2013.130 Published online by Cambridge University Press

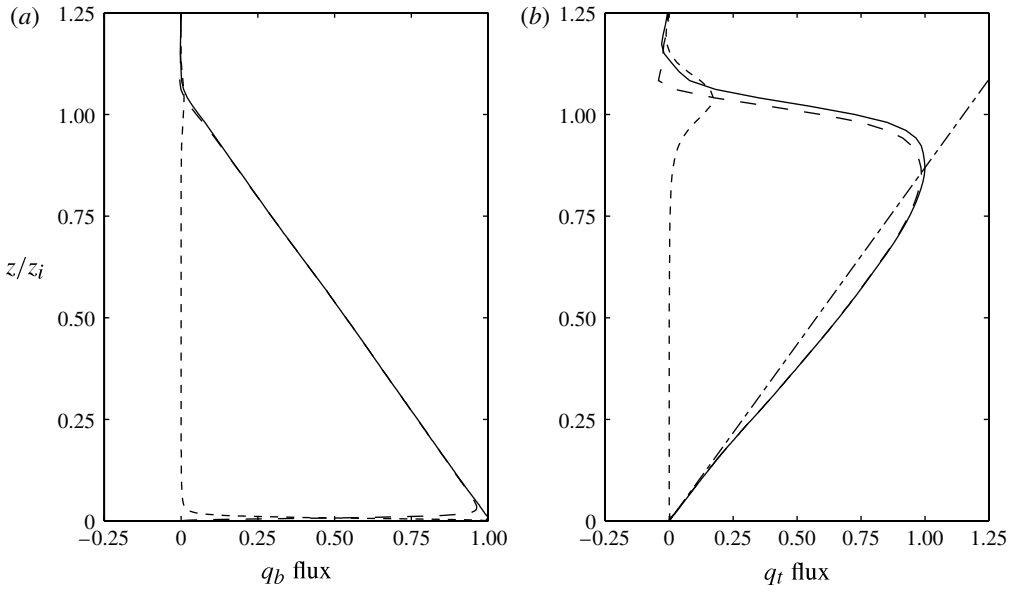


FIGURE 6. Vertical scalar flux for (*a*) q_b and (*b*) q_t. Solid line, total scalar flux; long dashed line, turbulent flux; short dashed line, viscous flux. The dot-dashed line indicates linear relationship between zero-flux wall and maximum top-down flux.

While it is convenient to normalize θ and q_b by the surface value of the viscous flux, such an operation is not possible for q_t since both the turbulent and viscous fluxes at $z = 0$ are zero. Instead, the total flux

$$Q_{q_t} = \overline{w'q_t'} - \frac{1}{ReSc}\frac{\partial q_t}{\partial z} \tag{3.9}$$

is normalized by $Q_{q_t,1}$ where

$$Q_{q_t,1} = \min(Q_{q_t}). \tag{3.10}$$

Note that, for the distribution of q_t shown in figure 3, both the turbulent and viscous fluxes will be negative over the entire mixed layer as the scalar is transported downwards towards the wall. The maximum of $Q_{q_t}/Q_{q_t,1}$ is found to occur at $z/z_i = 0.87$, which correlates very well with the crossover point where Q_θ goes from positive to negative flux. Unlike Q_θ or Q_{q_b}, the flux profile of a top-down process is not linear. Wyngaard & Brost (1984) attributed this to deepening of the ABL with time; this growth of the mixed layer is clearly seen in the water-tank experiments of Piper *et al.* (1995). The peak in viscous flux occurs just above the inversion ($z/z_i \approx 1.04$). At this point the turbulent and viscous fluxes are nearly equal in amplitude and greater than 17 % of $Q_{q_t,1}$. Whereas viscous effects are relevant only in a very thin layer at the wall for bottom-up diffusion, both viscous and turbulent fluxes play an important role at the temperature inversion for the top-down processes given the low Reynolds number of the simulation.

A comparison between the current DNS and other LES is provided in table 2. The Reynolds number based on convective scales is defined as $Re_c = w_* z_i/\nu$ and the

https://doi.org/10.1017/jfm.2013.130 Published online by Cambridge University Press

	Type	Re_c	u_*/w_*	Ri	$-z_i/L$
DNS (present work)	SW	4473	0.203	55.5	49.1
Patton *et al.* (2003)	RW	—	0.252	—	24.9
Patton *et al.* (2003)	C	—	0.282	—	17.8
Piper *et al.* (1995)	WT	1000–2000	—	29	—
Moeng & Wyngaard (1984)	RW	—	0.350	54	10
Wyngaard & Brost (1984)	RW	—	0.184	—	64

TABLE 2. Simulation parameters. Type codes: SW, smooth wall; WT, water-tank experiment; RW, rough-wall LES; and C, canopy LES.

Richardson number is

$$Ri = \frac{z_i/\delta_E}{(w_*/U_g)^2}\Delta\theta \tag{3.11}$$

in terms of dimensionless quantities. Note that $\Delta\theta$ is the jump in potential temperature across the entrainment layer. Despite the fact that our DNS is at a substantially lower Reynolds number in comparison with atmospheric LES studies, all other flow parameters are comparable to rough-wall LES conditions. In terms of the convective Reynolds number, the DNS is close to the water dye experiments of Piper *et al.* (1995).

4. Characteristics of turbulence

The use of DNS confines the present simulation to the low-Reynolds-number regime. Defining the Taylor micro-scale as

$$\lambda = \sqrt{\frac{15\nu u'}{\varepsilon}}, \tag{4.1}$$

a Reynolds number Re_λ is formed such that

$$Re_\lambda = \frac{\lambda u'}{\nu}, \tag{4.2}$$

where $u' = \overline{u'u'}^{1/2}$. For the present case, the maximum Reynolds number based on the Taylor micro-scale is $Re_\lambda \approx 190$. This is substantially lower than actual atmospheric dynamics, where Re_λ is approximately 10 000 (Dhruva, Tsuji & Sreenivasan 1997), but similar features between this low-Reynolds-number simulation and high-Reynolds-number flows are evident as described below.

The turbulence generated by the simulation is a consequence of vigorous surface heating. In comparison with neutral Ekman layer simulations (Coleman *et al.* 1990; Miyashita *et al.* 2006; Waggy *et al.* 2011; Marlatt *et al.* 2012), there are several distinct differences noted in the turbulence characteristics. Figure 7 shows the variances of velocity and temperature fluctuations where the temperature fluctuations have been normalized by the characteristic temperature θ_*,

$$\theta_* = \frac{Q_{\theta,0}}{w_*}, \tag{4.3}$$

https://doi.org/10.1017/jfm.2013.130 Published online by Cambridge University Press

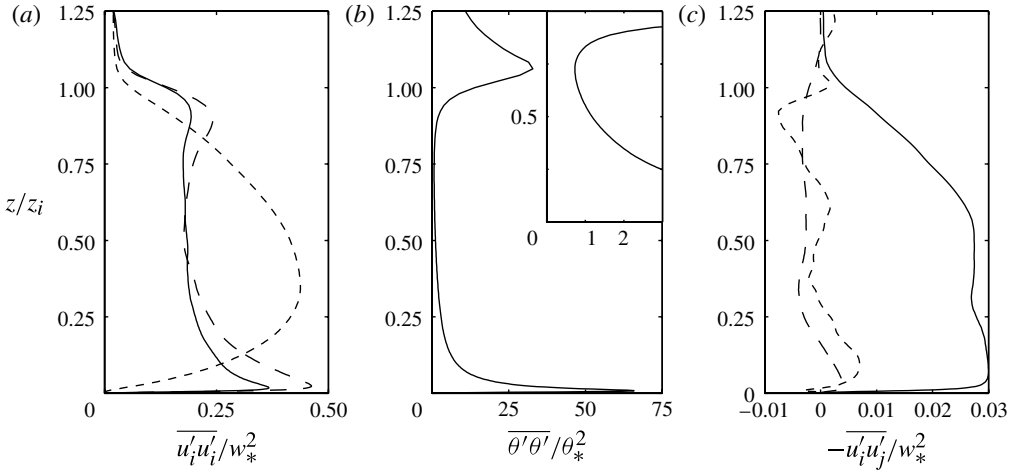


FIGURE 7. Second-order moments: (*a*) solid line, $\overline{u'u'}$; long dashed line, $\overline{v'v'}$; short dashed line, $\overline{w'w'}$; (*b*) $\overline{\theta'\theta'}$, inset shows details through mixed layer; (*c*) solid line, $-\overline{u'w'}$; long dashed line, $-\overline{v'w'}$; short dashed line, $-\overline{u'v'}$.

and $Q_{\theta,0}$ is the surface heat flux. Under neutral stratification, the streamwise normal stress dominates the flow, as production of $\overline{u'u'}$ is the primary turbulent energy source (Marlatt *et al.* 2012). As unstable buoyant forcing increases, the flow is dominated less by shear and more by buoyant production of energy (Waggy 2012). In figure 7(*a*), $\overline{w'w'}$ is the primary velocity variance through the mixed layer; the maximum value of $\overline{w'w'}/w_*^2 \approx 0.44$ is close to the values found by the laboratory model of Willis & Deardorff (1974), $0.40 < \max(\overline{w'w'}/w_*^2) < 0.55$, and the LES of Schmidt & Schumann (1989), $\max(\overline{w'w'}/w_*^2) \approx 0.41$.

The two horizontal velocity variances have maxima near the surface and close to the inversion. Both $\overline{u'u'}$ and $\overline{v'v'}$ are significantly lower than the vertical velocity variance; the profiles obtained agree closely with the LES study of the strongly convective, non-rotating boundary layer by Schmidt & Schumann (1989).

The variance of the temperature fluctuations shown in figure 7(*b*) demonstrates the inadequacy of using θ_* to normalize the temperature (see Moene, Michels & Holtslag 2006). A difference of almost two orders of magnitude exists between the near-wall maximum and the minimum found near the top of the mixed layer (where $\overline{\theta'\theta'}/\theta_*^2 \approx 1$).

Momentum fluxes are shown in figure 7(*c*). The primary covariance term $-\overline{u'w'}$ is the dominant Reynolds shear stress in the flow and exhibits a positive value throughout the mixed layer. The negative of the Reynolds stress is shown here since a negative stress, in association with a positive velocity gradient, produces turbulent kinetic energy. Apart from the region close to the wall, the spanwise covariance is negative. Nevertheless, both $\overline{u'w'}$ and $\overline{v'w'}$ act to produce turbulent energy near the wall. The secondary covariance $-\overline{u'v'}$ does not directly appear in the energy production term; however, this term is important for inter-component energy redistribution. As seen in figure 7(*c*), $-\overline{u'v'}$ is roughly symmetric about $z/z_i \approx 0.5$.

The skewness of the vertical velocity and potential temperature are defined by

$$S_w = \overline{w'^3}/\overline{w'^2}^{3/2} \tag{4.4}$$

https://doi.org/10.1017/jfm.2013.130 Published online by Cambridge University Press

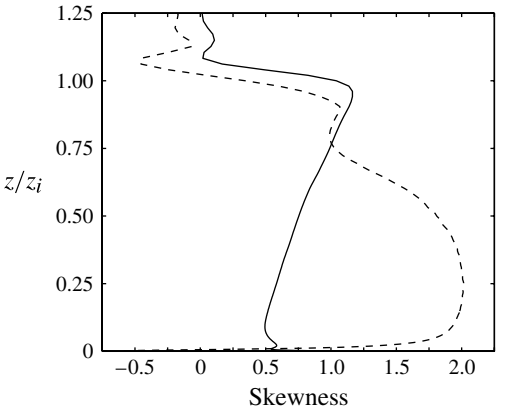


FIGURE 8. Skewness of vertical velocity (solid) and potential temperature (dashed).

and

$$S_\theta = \overline{\theta'^3}/\overline{\theta'^2}^{3/2}, \tag{4.5}$$

respectively. Distributions for each are shown across the mixed layer in figure 8. That for S_w demonstrates a positive skewness that increases linearly throughout the mixed layer; the peak skewness is $S_w \approx 1.16$ and occurs just below $z = z_i$. Although this value agrees with convective boundary-layer LES data (Mason 1989; Mironov *et al.* 2000; Gryanik & Hartmann 2002; Sullivan & Patton 2011), it is not representative of ABL conditions (LeMone 1990; Moeng & Rotunno 1990; Lenschow *et al.* 2012). In the ABL, LeMone (1990) argues that very large-scale features of size > 10 km with near-zero skewness prohibit further increases in skewness in the vicinity of z_i, and therefore a decrease in skewness should occur as $z \to z_i$. The current DNS, as well as the LES studies noted earlier, do not capture these very large scales resulting in the observed increased skewness near the inversion. The skewness of potential temperature only mimics the behaviour of S_w when $z/z_i > 0.75$. For most of the mixed layer, S_θ is significantly larger than S_w; similar behaviour is seen in the work of Gryanik & Hartmann (2002).

Instantaneous vertical velocity and temperature contours give an indication of typical turbulent structures found throughout the flow field. Near the wall ($z/z_i \approx 0.1$), figure 9 shows the existence of worm-like structures elongated in the x direction and aligned with the direction of local shear. Similar elongation in the direction of shear is seen in both the Ekman layer under neutral stratification (Zikanov, Slinn & Dhanak 2003; Waggy *et al.* 2011) as well as in turbulent channel-flow LES results (Moin & Kim 1982). Considering the mixed layer, figure 10 shows that buoyant plumes dominate the turbulence field. High-temperature regions correspond closely to positive vertical velocities; less intense downdraught areas tend to surround the positive regions. This indicates that the stratification is too severe for roll vortices to exist (Coleman & Ferziger 1994). Above the inversion, the coupling between $+w'$ and $+\theta'$ is inverted (figure 11). Regions where $\theta' \ll 0$ tend to be associated with upward-moving fluid. This is expected, as high-momentum fluid carries cold underlying fluid up through the temperature inversion.

https://doi.org/10.1017/jfm.2013.130 Published online by Cambridge University Press

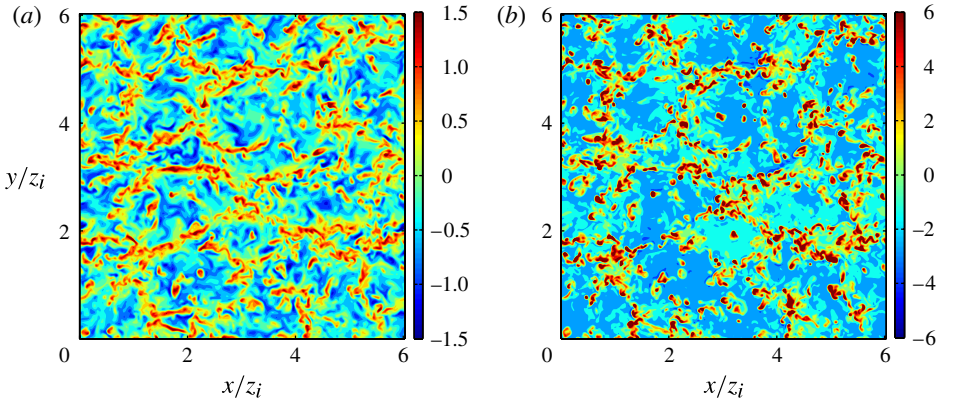


FIGURE 9. Instantaneous (*a*) w' and (*b*) θ'; here $z/z_i = 0.11$.

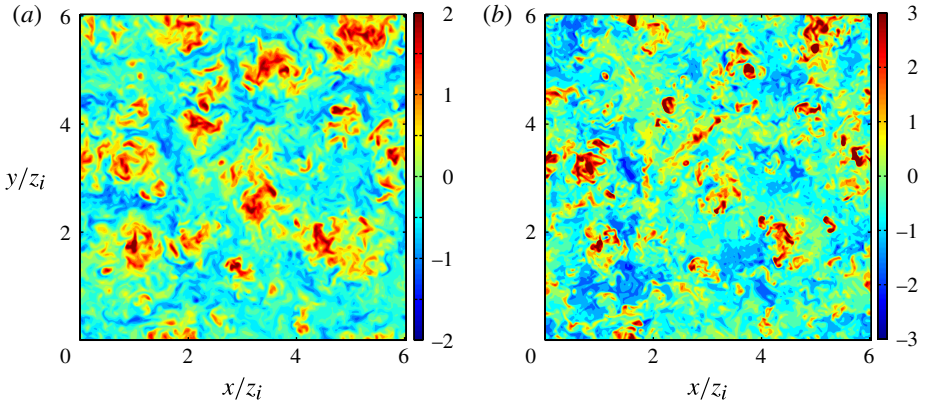


FIGURE 10. Instantaneous (*a*) w' and (*b*) θ'; here $z/z_i = 0.70$.

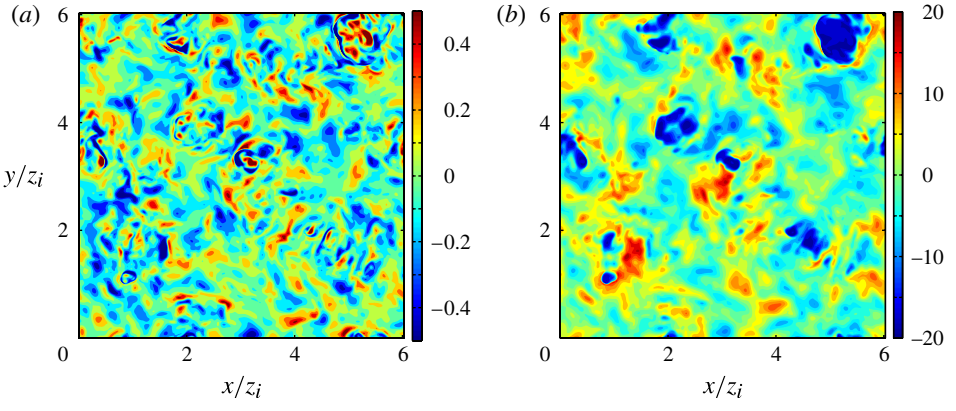


FIGURE 11. Instantaneous (*a*) w' and (*b*) θ'; here $z/z_i = 1.04$.

https://doi.org/10.1017/jfm.2013.130 Published online by Cambridge University Press

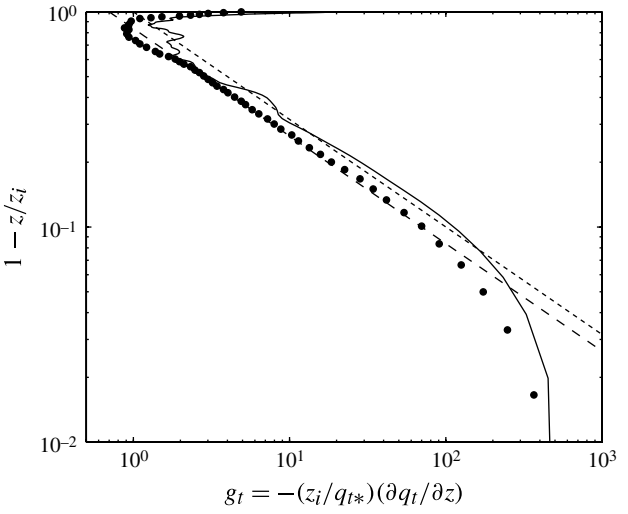


FIGURE 12. Gradient of mean top-down scalar distribution. Solid line, DNS; long dashed line, equation (5.5), $C_t = 0.7$; short dashed line, equation (5.5), $C_t = 1$; filled circles, LES with canopy (see Patton *et al.* 2003).

5. Top-down diffusion

In order for a scalar to exhibit pure top-down diffusion, the scalar gradient at $z = 0$ must be identically zero to ensure both turbulent and viscous fluxes vanish at the wall. This is accomplished by imposing a zero-gradient boundary condition on the top-down scalar q_t. Consequently, the steepest gradients in q_t occur near the inversion and decay as $z \to 0$.

A simple mixing length hypothesis for the scalar flux of q_t can be constructed as follows:

$$Q_{q_t} = -K_t \frac{\partial q_t}{\partial z}, \tag{5.1}$$

where K_t is the eddy diffusivity for a top-down scalar. Solving for K_t yields

$$K_t = -\frac{Q_{q_t}}{\partial q_t/\partial z}. \tag{5.2}$$

A dimensionless scalar gradient can be defined as

$$g_t = -\frac{z_i}{q_{t*}} \frac{\partial q_t}{\partial z}, \tag{5.3}$$

where q_{t*} is a characteristic scalar value defined as

$$q_{t*} = \frac{Q_{q_t,1}}{w_*}. \tag{5.4}$$

The dimensionless mean scalar gradient g_t obtained from the present DNS is shown in figure 12 and is compared with the best-fit curve of Moeng & Wyngaard (1984) defined as

$$g_t \approx C_t \, (1 - z/z_i)^{-2} \tag{5.5}$$

https://doi.org/10.1017/jfm.2013.130 Published online by Cambridge University Press

with $C_t = 1$; Moeng & Wyngaard (1984) chose $C_t = 0.7$ as a fit to their LES data. The data show good agreement between their approximation and the DNS data for $0.1 < z/z_i < 0.95$. Approaching the wall, the gradient function demonstrates a deviation from (5.5) as g_t increases. Similar near-wall behaviour for a top-down scalar is noted by Piper *et al.* (1995). In their work, Patton *et al.* (2003) demonstrated that adding a tree canopy to their LES had little effect on g_t. Our results validate their findings: the top-down diffusion of a scalar is not a function of surface roughness. As shown in figure 12, only a slight increase in the gradient function throughout the mixed layer is noted for the low-Reynolds-number DNS. This increase in g_t indicates a small decrease in mixing efficiency. The difference in the amplitude of g_t is likely to be a consequence of the Reynolds number as opposed to the surface roughness, given the consistency of the offset throughout the mixed layer. Nevertheless, the similarity between the smooth-wall, low-Reynolds-number DNS and the rough-wall, atmospheric LES suggests that, in the mixed layer, g_t is only weakly influenced by surface roughness, large variations in the Reynolds number, or the degree of unstable forcing.

If a linear relationship between the scalar flux and height in the mixed layer is assumed, such that the maximum flux occurs at the temperature inversion, then

$$\frac{Q_{q_t}}{Q_{q_t,1}} \approx \frac{z}{z_i}. \tag{5.6}$$

Combining (5.2)–(5.6) with $C_t = 1$, the predicted eddy diffusivity based on a linear flux profile is given by

$$\frac{K_t}{w_* z_i} \approx \left(\frac{z}{z_i}\right)\left(1 - \frac{z}{z_i}\right)^2. \tag{5.7}$$

Figure 13 compares this cubic polynomial approximation along with our DNS results for the eddy diffusivity and scalar flux, and indicates that (5.7) and the DNS results are in relatively good agreement. The K_t value is under-predicted through the mixed layer and over-predicted in the very near-wall region. From figure 12 it is clear that the near-wall deviation is caused by an under-estimation of the velocity gradient at the lower boundary (top of figure). As shown in figure 13(*b*), the location of the maximum scalar flux, which is computed via (5.1) and (5.7), is correctly captured ($z/z_i \approx 0.88$) and the magnitude of the flux is only off by approximately 3.5 %. For $0.25 < z/z_i < 0.85$, the total top-down flux is marginally under-predicted. This is partially a consequence of assuming that the flux is linear, with a maximum flux at the inversion (5.6). A small improvement through the mixed layer is obtained by fitting a linear trend between the wall (zero flux) and the height at which $Q_{q_t}/Q_{q_t,1} = 1$. However, the height at which this occurs ($z/z_i = 0.869$ for this case) may not be universal and could demonstrate dependence on Reynolds number or the level of unstable buoyant forcing. Finally, the parametrization of g_t by (5.5) dictates that the eddy diffusivity is zero at $z = z_i$. In fact, both the turbulent and viscous fluxes are substantial at the inversion. The total scalar flux from the DNS reaches zero at approximately $z/z_i = 1.13$.

6. Bottom-up diffusion

Since a top-down diffusion process exhibits zero flux at the wall, a true bottom-up process should exhibit zero flux near the temperature inversion. Wyngaard & Brost (1984) explicitly enforced a zero-flux condition at the top of the mixed layer (as

https://doi.org/10.1017/jfm.2013.130 Published online by Cambridge University Press

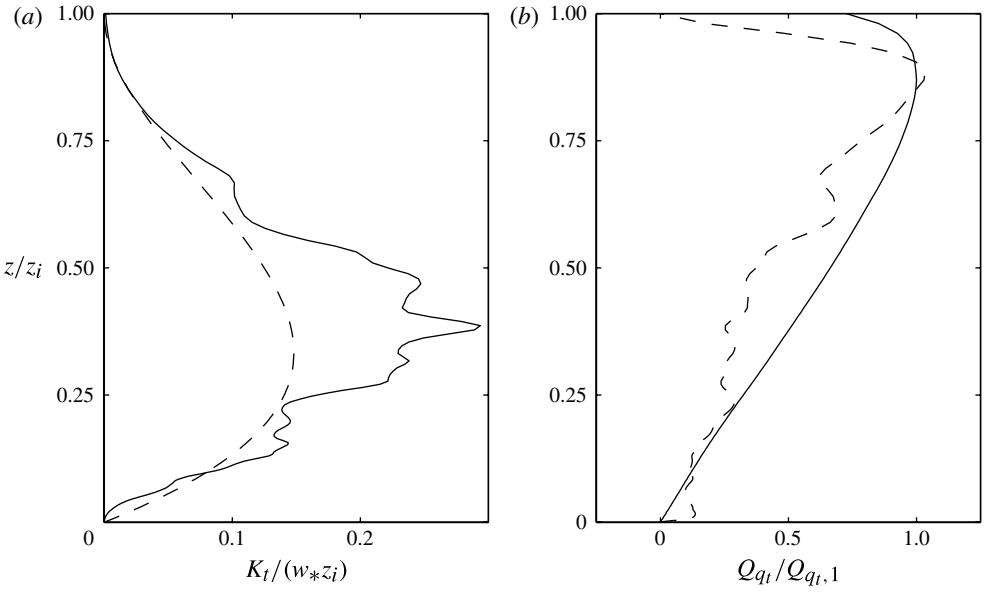


FIGURE 13. (*a*) Eddy diffusivity and (*b*) scalar flux for top-down scalar. Solid line, DNS; dashed line, equation (5.7).

determined by the maximum amplitude of their top-down scalar flux). Moeng & Wyngaard (1984) and Piper *et al.* (1995) extract the bottom-up scalar gradient using the top-down scalar and a scalar (or temperature) that exhibits both top-down and bottom-up diffusion. Although results from the DNS (see figure 6) show that Q_{q_b} is small at z_i, indicating only a small contribution from top-down diffusion, the effect of top-down diffusion on the bottom-up scalar has been removed, so a pure bottom-up process is captured.

As with the top-down scalar, the eddy diffusivity for a bottom-up process is given by

$$K_b = -\frac{Q_{q_b}}{\partial q_b/\partial z}, \tag{6.1}$$

and a dimensionless scalar gradient is defined as

$$g_b = -\frac{z_i}{q_{b*}}\frac{\partial q_b}{\partial z}, \tag{6.2}$$

where

$$q_{b*} = \frac{Q_{q_b,0}}{w_*}. \tag{6.3}$$

Top-down diffusion effects are removed using the assumption that the gradient of an arbitrary scalar has both top and bottom diffusion effects:

$$\frac{\partial c}{\partial z} = \frac{\partial c_b}{\partial z} + \frac{\partial c_t}{\partial z}. \tag{6.4}$$

https://doi.org/10.1017/jfm.2013.130 Published online by Cambridge University Press

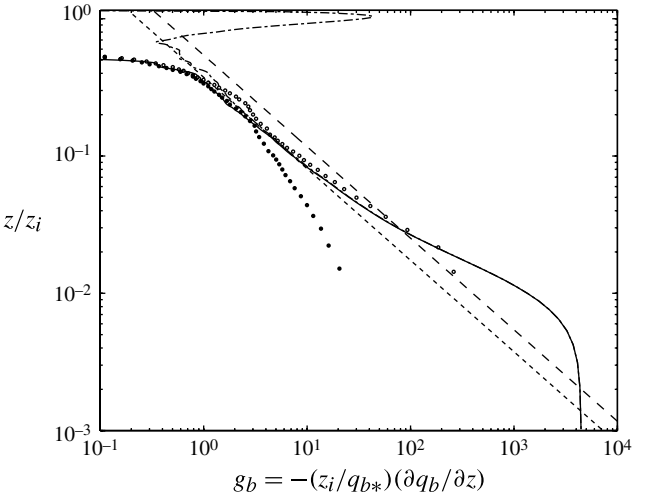


FIGURE 14. Gradient of mean bottom-up scalar distribution. Solid line, DNS (6.5); dot-dashed line, DNS (6.2); long dashed line, equation (6.6), $C_b = 0.4$; short dashed line, equation (6.6), $C_b = 0.23$; open circles, LES without canopy; filled circles, LES with canopy (see Patton *et al.* 2003).

The gradient of c_t has already been parametrized in figure 12, so g_b (minus top-down effects) is given by

$$g_b = -\frac{z_i w_*}{Q_{q_b,0}} \frac{\partial q_b}{\partial z} - \frac{Q_{q_b,1}}{Q_{q_b,0}} g_t. \tag{6.5}$$

The height at which $Q_{q_b,1}$ was taken corresponds to the point where $Q_{q_t}/Q_{q_t,1} = 1$. The gradient profile g_b is shown in figure 14. The model

$$g_b \approx C_b \left(\frac{z}{z_i}\right)^{-3/2} \tag{6.6}$$

of Wyngaard & Brost (1984) fits the scalar q_b data very well for $0.08 < z/z_i < 0.4$. For $z/z_i > 0.4$, the gradient function changes sign and (6.6) no longer holds. Interestingly, if top-down effects are not removed, i.e. $g_b = -(z_i w_*/Q_{q_b,0})\,\partial q_b/\partial z$, agreement between the model and DNS is evident up until $z/z_i \approx 0.7$ (dot-dashed curve in figure 14). The constant $C_b = 0.23$ used to fit our data is close to the value $C_b = 0.4$ used by Wyngaard & Brost (1984) for their LES data. Patton *et al.* (2003) notice enhanced mixing efficiency (a decrease in g_b) for flow with canopy in comparison to flow without. It is expected, then, that the smooth-wall DNS would also show an increase in g_b near the wall, as mixing from surface roughness is eliminated. However, the gradient function g_b closely aligns with their no-canopy results for $z/z_i > 0.02$. Thus, differences between bottom-up diffusion for a smooth and rough wall are limited to a very thin layer near the wall. Below $z/z_i = 0.02$, the smooth-wall results show a considerable increase in g_b through the viscous sublayer (note that $z/z_i = 0.01$ corresponds with $z^+ \approx 9.1$). For the Reynolds number of the DNS, the viscous sublayer is considerably thicker than that of rough-wall LES.

Both Moeng & Wyngaard (1984) and Piper *et al.* (1995) show $g_b \approx 0$ at $z/z_i \approx 0.5$–0.6 when g_b is deduced from other flow variables; this crossover point

https://doi.org/10.1017/jfm.2013.130 Published online by Cambridge University Press

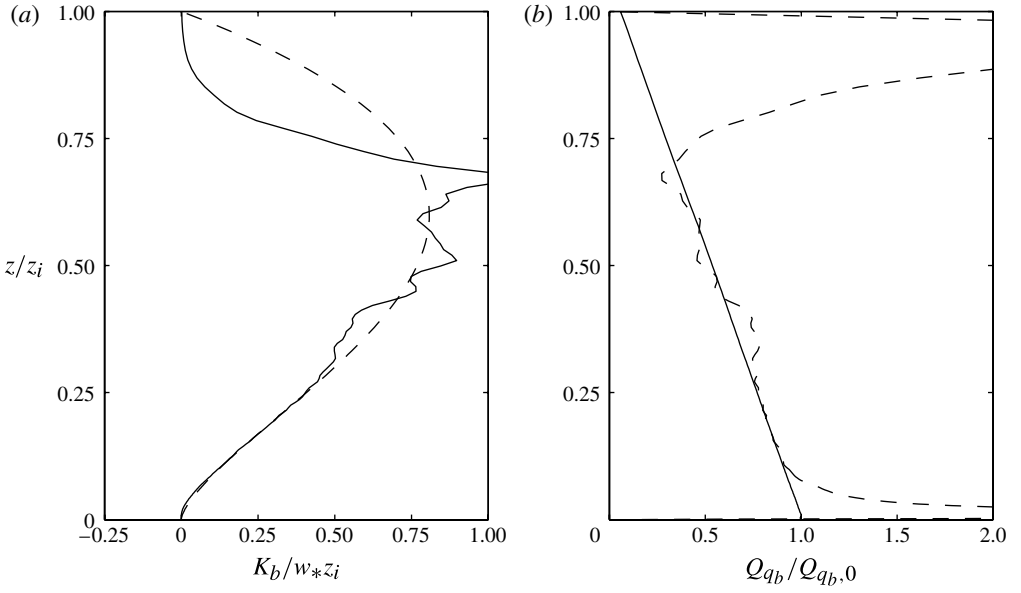


FIGURE 15. (*a*) Eddy diffusivity and (*b*) scalar flux for bottom-up scalar. Solid line, DNS; dashed line, equation (6.7).

is well captured by our DNS results. The gradient function in the bottom half of the mixed layer appears to be well represented by (6.6), as shown in figure 14. However, above $z/z_i > 0.6$ the gradient function model does not capture the sign change associated with pure bottom-up diffusion.

Combining (6.1), (6.6) and the approximation that $Q_{q_b}/Q_{q_b,0} \approx 1 - z/z_i$ yields the following model for the eddy diffusivity of a bottom-up scalar:

$$\frac{K_b}{w_* z_i} = \left(\frac{1}{0.23}\right)\left(1 - \frac{z}{z_i}\right)\left(\frac{z}{z_i}\right)^{3/2}. \tag{6.7}$$

Figure 15 compares the DNS and model eddy diffusivities (figure 15*a*) and resulting total scalar flux (figure 15*b*). Note that the turbulent flux $\overline{w'q'_b}$ has not had top-down effects removed. Once again, the model does well except for close to the inversion and near the wall, where the viscous sublayer is approached. It is expected that the model will perform better in the near-wall region as the Reynolds number increases. The over-prediction of the total flux near the inversion is probably a consequence of the presence of top-down diffusion in $\overline{w'q'_b}$ and not, necessarily, a Reynolds-number effect.

7. Variance and covariance functions

The gradient functions for top-down and bottom-up processes are useful in determining the vertical flux of a scalar in the mixed layer. While (1.1) relates the flux of a scalar to contributions from both top-down and bottom-up diffusion, the variance of a scalar c is a function of top-down diffusion, bottom-up diffusion and a cross-correlation between the two processes (Moeng & Wyngaard 1989):

$$\overline{c'c'} = \overline{c'_t c'_t} + 2\overline{c'_t c'_b} + \overline{c'_b c'_b}. \tag{7.1}$$

https://doi.org/10.1017/jfm.2013.130 Published online by Cambridge University Press

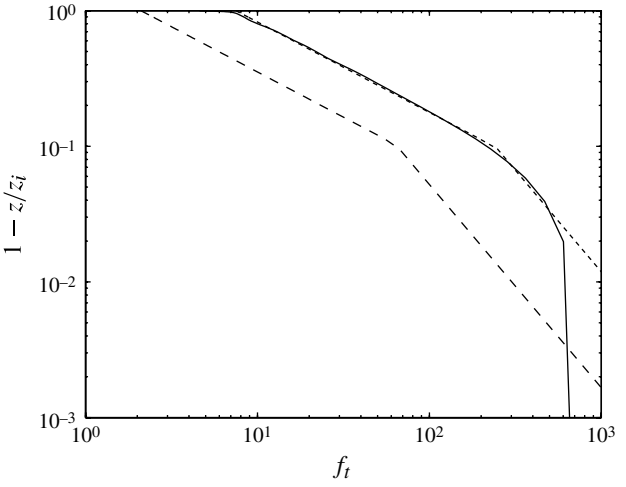


FIGURE 16. Scalar variance for top-down diffusion: solid line, DNS; long dashed line, equation (7.4*a*), $a_1 = 2.1$ and $a_2 = 14$; short dashed line, equation (7.4*a*), $a_1 = 7.5$ and $a_2 = 52$.

In an attempt to parametrize $\overline{c'c'}$, variance functions (denoted f_t, f_b and f_{tb} for top, bottom and mixed diffusion) can be formed for each term as follows:

$$\overline{c_t'c_t'} = q_{t*}^2 f_t \tag{7.2a}$$

$$\overline{c_t'c_b'} = q_{t*}q_{b*}f_{tb} \tag{7.2b}$$

$$\overline{c_b'c_b'} = q_{b*}^2 f_b. \tag{7.2c}$$

If the above variance functions are universal (independent of Reynolds number or the level of unstable buoyant forcing), then the variance of some arbitrary scalar could be determined if the strength of top-down diffusion relative to bottom-up diffusion is known. Letting $R = Q_{c,1}/Q_{c,0}$ be the ratio of the entrainment flux to surface flux, the variance for an arbitrary scalar c can be approximated as (Moeng & Wyngaard 1984)

$$\frac{\overline{c'c'}}{c_*^2} = R^2 f_t + 2Rf_{tb} + f_b, \tag{7.3}$$

where $c_* = Q_{c,0}/w_*$, the total surface flux divided by the convective velocity.

Variance of the top-down scalar for the present DNS is shown in figure 16. Moeng & Wyngaard (1984) fitted their LES data with empirical functions

$$f_t = a_1\left(1 - \frac{z}{z_i}\right)^{-3/2}, \quad z/z_i < 0.9, \tag{7.4a}$$

$$f_t = a_2\left(1 - \frac{z}{z_i}\right)^{-2/3}, \quad z/z_i > 0.9, \tag{7.4b}$$

and specified $a_1 = 2.1$ and $a_2 = 14$ to fit their data. While the $-3/2$ relation in the mixed layer appears qualitatively correct, a large increase in a_1 is required to fit our smooth-wall results. Moeng & Wyngaard (1989) demonstrate via LES that an increase in the scalar variance occurs with an increase in grid resolution, since only resolved

https://doi.org/10.1017/jfm.2013.130 Published online by Cambridge University Press

scales are considered when computing the scalar variance. With increased resolution, the best fit to their results is obtained when $a_1 = 3.1$ (see also Patton *et al.* 2003). Given that this DNS captures the majority of significant length scales, it is believed that the larger constant required to fit the present DNS data is due, in part, to the increased range of resolved length scales. Additionally, the variability in a_1 indicates that the scaling between $\overline{q_t' q_t'}$ and q_{t*}^2 may not be universal. Referring to the definition of q_{t*} in (5.4), this dimensionless parameter is a function of the minimum scalar flux and the convective velocity w_*. However, w_* is defined in terms of the surface heat flux and the inversion height (3.1); these flow parameters are independent of the scalar distribution, as there is no feedback from the scalar field to the fluid. Thus, the constants a_1 and a_2 are probably dependent upon the specific flow conditions, notably, the gradient of q_t near the entrainment layer.

Because of coarse resolution in their LES near the inversion, the fit that Moeng & Wyngaard (1984) propose for $z/z_i > 0.9$ is relatively uncertain. Our DNS also has a coarse resolution near the inversion (in comparison to the near-wall region), but mesh points closer to the inversion were captured, allowing for a better approximation of f_t near z_i. The $-2/3$ relation does reasonably well at capturing scalar variance near the inversion. However, (7.4*a*) assumes that $\overline{q_t' q_t'} \to \infty$ as $z/z_i \to 1$ and will perform poorly near the inversion, as the scalar variance is bounded.

The bottom-up scalar q_b and temperature θ were used to solve for f_b and f_{tb}. Since f_t is known, a two-equation system for f_b and f_{tb} is formed from (7.3) and solved using variances $\overline{q_b' q_b'}$ and $\overline{\theta'\theta'}$ (see Moeng & Wyngaard 1984). The scalar variances for a bottom-up process are approximated by Moeng & Wyngaard (1984) as

$$f_b = b_1 \left(\frac{z}{z_i} \right)^{-2/3}, \quad z/z_i < 0.9, \tag{7.5a}$$

$$f_b = b_2 \left(\frac{z}{z_i} \right)^{-5/4}, \quad z/z_i > 0.9. \tag{7.5b}$$

The constants are given by $b_1 = 1.8$ and $b_2 = 0.47$. Moeng & Wyngaard (1989) adjust this model by changing the exponent of (7.5*a*) to be -0.9. Figure 17 demonstrates that the piecewise function given by (7.5) does not correlate well with the DNS results. Instead of a two-step function, it appears that the variance is better approximated by a single relationship:

$$f_b \approx 0.91 \left(\frac{z}{z_i} \right)^{-0.95}. \tag{7.6}$$

The exponent -0.95 is close to the modified exponent of Moeng & Wyngaard (1989), though they still employ a piecewise function to model the variance near the wall ($z/z_i < 0.1$). Not only does (7.6) fit our DNS for the majority of the mixed layer, there is very good agreement for $z/z_i < 0.1$ up until $z/z_i < 0.01$, where viscous effects dominate ($z^+ \approx 9.1$).

The covariance between the top-down and bottom-up scalars is shown in figure 18. Given the small amplitude of f_{tb} relative to the variance functions, the covariance is commonly modelled as a constant. Moeng & Wyngaard (1989) demonstrate an increase in the magnitude of f_{tb} with an increase in LES resolution. As their calculation of f_{tb} does not account for subgrid effects, correlation is lost in subgrid scales without a fine resolution. Patton *et al.* (2003) utilized a nested grid LES to better resolve the wall region and found a maximum covariance of $f_{tb} \approx 4.5$ with a

https://doi.org/10.1017/jfm.2013.130 Published online by Cambridge University Press

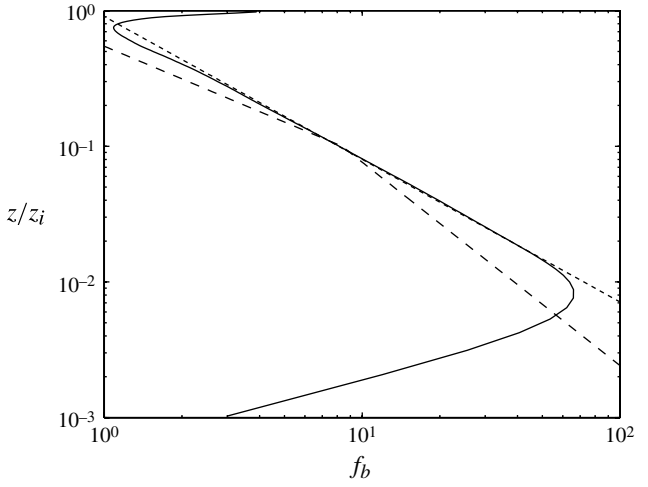


FIGURE 17. Scalar variance for bottom-up diffusion: solid line, DNS; long dashed line, $b_1 = 1.8$ and $b_2 = 0.47$; short dashed line, $f_t \approx 0.91\,(z/z_i)^{-0.95}$.

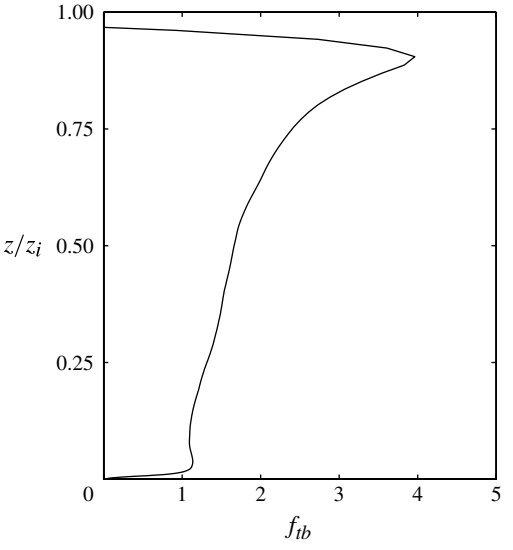


FIGURE 18. Scalar covariance: solid line, DNS.

tree canopy and $f_{tb} \approx 4.0$ without. Our DNS results give a maximum covariance of $f_{tb} \approx 3.96$ at $z/z_i \approx 0.9$. Therefore, the smooth-wall results of this DNS, the rough-wall LES of Moeng & Wyngaard (1984, 1989) and Patton *et al.* (2003) and the canopy results of Patton *et al.* (2003) show that the scalar covariance may vary little with surface roughness and that small-scale effects play a substantial role in f_{tb}.

8. Conclusions

A DNS of top-down and bottom-up diffusion in the convective boundary layer at $Re_c = 4473$ and $z_i/L = -49.1$ was performed for a smooth wall. Two passive scalars

https://doi.org/10.1017/jfm.2013.130 Published online by Cambridge University Press

were initialized in a fully turbulent flow field and integrated forwards until well mixed. The heat flux profile is linear between $0 \leqslant z/z_i \leqslant 1$ where z_i corresponds with the point of minimum heat flux. The contribution from viscous flux is substantial only in the viscous sublayer and above the inversion.

The scalar q_t is a function of top-down diffusion only, as a zero-gradient boundary condition is imposed at the surface. Like Wyngaard & Brost's (1984) results, the total flux of q_t is not linear but exhibits a slight curvature. This nonlinearity has been attributed to the deepening of the ABL. As the temperature inversion is approached, viscous flux increases and is not negligible (as it is through the mixed layer) for the low-Reynolds-number case presented here. The gradient function of q_t is well represented by the model of Moeng & Wyngaard (1984) except at the inversion (where the model is expected to perform poorly) and at the wall. Though resigned to a thin region, a large increase in the scalar gradient occurs as $z \to 0$.

Since pure bottom-up scalar diffusion could not be replicated, top-down effects were removed from q_b by means of the potential temperature (Moeng & Wyngaard 1984; Piper *et al.* 1995). The model of Wyngaard & Brost (1984) represents the gradient for approximately the bottom half of the mixed layer (apart from the very near-wall region). The gradient function switches sign for $z/z_i > 0.6$ and is therefore not represented by the empirical fit proposed by Wyngaard & Brost (1984). If the small effects of top-down diffusion on q_b are not removed, agreement with Wyngaard & Brost's (1984) results is extended to $z/z_i \approx 0.7$. The bottom-up gradient function was found to correlate very closely with the rough-wall LES of Patton *et al.* (2003) without a tree canopy. Differences (notably, an increase in g_b) are confined to a very thin layer at the lower boundary.

Both the top-down and mixed scalar variances (f_t and f_{tb}, respectively) show little surface-roughness or Reynolds-number effects in comparison with the results of Patton *et al.* (2003). However, a new model for the pure bottom-up scalar variance ($f_b \propto (z/z_i)^{-0.95}$) is proposed. The exponent -0.95 is close to that in the model of Moeng & Wyngaard (1989), who use a constant of -0.9. Here we replace the two piecewise functions of Moeng & Wyngaard (1984, 1989) with a single expression. With the new model, the variance is accurately captured from the top of the viscous sublayer to $z/z_i \approx 0.9$.

Acknowledgements

Support for S.B.W. was provided by the Graduate Assistantship in Areas of National Need Fellowship through the Aerospace Engineering Sciences Department at the University of Colorado, Boulder. This research was supported by an allocation of advanced computing resources provided by the National Science Foundation. The computations were performed on Kraken at the National Institute for Computational Sciences (http://www.nics.tennessee.edu/). S.B. was supported, in part, by NSF Award No. 1131802.

REFERENCES

ADRIAN, R. J., FERREIRA, R. T. D. S. & BOBERG, T. 1986 Turbulent thermal convection in wide horizontal fluid layers. *Exp. Fluids* **4**, 121–141.

ANDERSON, D. A., TANNEHILL, J. C. & PLETCHER, R. H. 1984 *Computational Fluid Mechanics and Heat Transfer*. Hemisphere.

COLEMAN, G. N. & FERZIGER, J. H. 1994 A numerical study of the convective boundary layer. *Boundary-Layer Meteorol.* **70**, 247–272.

https://doi.org/10.1017/jfm.2013.130 Published online by Cambridge University Press

COLEMAN, G. N., FERZIGER, J. H. & SPALART, P. R. 1990 A numerical study of the Ekman layer. *J. Fluid Mech.* **213**, 313–348.

DEARDORFF, J. W. 1972 Numerical investigation of neutral and unstable planetary boundary layers. *J. Atmos. Sci.* **29**, 91–115.

DEARDORFF, J. W. & WILLIS, G. E. 1985 Further results from a laboratory model of the convective planetary boundary layer. *Boundary-Layer Meteorol.* **32**, 205–236.

DHRUVA, B., TSUJI, Y. & SREENIVASAN, K. S. 1997 Transverse structure functions in high-Reynolds-number turbulence. *Phys. Rev.* E **56** (5), 4928–4930.

GRYANIK, V. M. & HARTMANN, J. 2002 A turbulence closure for the convective boundary layer based on a two-scale mass-flux approach. *J. Atmos. Sci.* **59**, 2729–2744.

JONKER, H. J. J., SULLIVAN, P. P., PATTON, E. G. & VAN REEUWIJK, M. 2010 Direct numerical simulation of entrainment in dry convective boundary layers. In *Proceedings of the 19th Symposium on Boundary Layers and Turbulence, Keystone, CO*. American Meteorological Society.

LEMONE, M. A. 1973 The structure and dynamics of horizontal roll vortices in the planetary boundary layer. *J. Atmos. Sci.* **30**, 1077–1091.

LEMONE, M. A. 1990 Some observations of vertical velocity skewness in the convective boundary layer. *J. Atmos. Sci.* **47**, 1163–1169.

LENSCHOW, D. H., LOTHON, M., MAYOR, S. D., SULLIVAN, P. P. & CANUT, G. 2012 A comparison of higher-order vertical velocity moments in the convective boundary layer from lidar with *in situ* measurements and large-eddy simulation. *Boundary-Layer Meteorol.* **143**, 107–123.

MARLATT, S., WAGGY, S. & BIRINGEN, S. 2010 Direct numerical simulation of the turbulent Ekman layer: turbulent energy budgets. *J. Thermophys. Heat Transfer* **24**, 544–555.

MARLATT, S., WAGGY, S. & BIRINGEN, S. 2012 Direct numerical simulation of the turbulent Ekman layer: evaluation of closure models. *J. Atmos. Sci.* **69**, 1106–1117.

MASON, P. J. 1989 Large-eddy simulation of the convective atmospheric boundary layer. *J. Atmos. Sci.* **46** (11), 1492–1516.

MIRONOV, D. V., GRYANIK, V. M., MOENG, C. H., OLBERS, D. J. & WARNCKE, T. H. 2000 Vertical turbulence structure and second-moment budgets in convection with rotation: a large-eddy simulation study. *Q. J. R. Meteorol. Soc.* **126** (563), 477–515.

MIYASHITA, K., IWAMOTO, K. & KAWAMURA, H. 2006 Direct numerical simulation of the neutrally stratified turbulent Ekman boundary layer. *J. Earth Simulator* **6**, 3–15.

MOENE, A. F., MICHELS, B. I. & HOLTSLAG, A. A. M. 2006 Scaling variances of scalars in a convective boundary layer under different entrainment regimes. *Boundary-Layer Meteorol.* **120**, 257–274.

MOENG, C. H. & ROTUNNO, R. 1990 Vertical-velocity skewness in the buoyancy-driven boundary layer. *J. Atmos. Sci.* **47**, 1149–1162.

MOENG, C. H. & WYNGAARD, J. C. 1984 Statistics of conservative scalars in the convective boundary layers. *J. Atmos. Sci.* **41**, 3161–3169.

MOENG, C. H. & WYNGAARD, J. C. 1988 Spectral analysis of large-eddy simulations of the convective boundary layer. *J. Atmos. Sci.* **45**, 3573–3587.

MOENG, C. H. & WYNGAARD, J. C. 1989 Evaluation of turbulent transport and dissipation closures in second-order modelling. *J. Atmos. Sci.* **46**, 2311–2330.

MOIN, P. & KIM, J. 1982 Numerical investigation of turbulent channel flow. *J. Fluid Mech.* **118**, 341–377.

OBUKHOV, A. M. 1971 Turbulence in an atmosphere with a non-uniform temperature. *Boundary-Layer Meteorol.* **2**, 7–29.

PATTON, E. G., SULLIVAN, P. P. & DAVIS, K. J. 2003 The influence of a forest canopy on top-down and bottom-up diffusion in the planetary boundary layer. *Q. J. R. Meteorol. Soc.* **129**, 1415–1434.

PIPER, M., WYNGAARD, J. C., SNYDER, W. H. & LAWSON, R. E. JR. 1995 Top-down, bottom-up diffusion experiments in a water convection tank. *J. Atmos. Sci.* **52**, 3607–3619.

SCHMIDT, H. & SCHUMANN, U. 1989 Coherent structure of the convective boundary layer derived from large-eddy simulations. *J. Fluid Mech.* **200**, 511–562.

https://doi.org/10.1017/jfm.2013.130 Published online by Cambridge University Press

SORBJAN, Z. 2004 Large-eddy simulations of the baroclinic mixed layer. *Boundary-Layer Meteorol.* **112**, 57–80.

SPALART, P. R., COLEMAN, G. N. & JOHNSTONE, R. 2008 Direct numerical simulation of the Ekman layer: a step in Reynolds number, and cautious support for a log law with a shifted origin. *Phys. Fluids* **20**, 101507.

SULLIVAN, P. P., MOENG, C. H., STEVENS, B., LENSCHOW, D. H. & MAYOR, S. D. 1998 Stucture of the entrainment zone capping the convective atmospheric boundary layer. *J. Atmos. Sci.* **55**, 3042–3064.

SULLIVAN, P. P. & PATTON, E. G. 2011 The effect of mesh resolution on convective boundary layer statistics and structures generated by large-eddy simulation. *J. Atmos. Sci.* **68**, 2395–2415.

WAGGY, S. B. 2012 Turbulent transport in the atmospheric boundary layer with application to wind farm dynamics. PhD thesis, University of Colorado, Boulder, CO.

WAGGY, S. B., KUCALA, A. M. & BIRINGEN, S. 2012 Parallel implementation of a Navier–Stokes solver: turbulent Ekman layer direct numerical simulation. In *Proceedings of the 50th AIAA Aerospace Sciences Meeting, Nashville*, AIAA-2012-0443.

WAGGY, S. B., MARLATT, S. & BIRINGEN, S. 2011 Direct numerical simulation of the turbulent Ekman layer: instantaneous flow structures. *J. Thermophys. Heat Transfer* **25**, 309–318.

WANG, W., DAVIS, K. J., YI, C., PATTON, E. G., BUTLER, M. P., RICCIUTO, D. M. & BAKWIN, P. S. 2007 A note on the top-down and bottom-up gradient functions over a forested site. *Boundary-Layer Meteorol.* **124**, 305–314.

WILLIS, G. E. & DEARDORFF, J. W. 1974 A laboratory model of the unstable planetary boundary layer. *J. Atmos. Sci.* **31**, 1297–1307.

WYNGAARD, J. C. 2010 *Turbulence in the Atmosphere*, p. 49. Cambridge University Press.

WYNGAARD, J. C. & BROST, R. A. 1984 Top-down and bottom-up diffusion of a scalar in the convective boundary layer. *J. Atmos. Sci.* **41**, 102–112.

ZIKANOV, O., SLINN, D. N. & DHANAK, M. R. 2003 Large-eddy simulations of the wind-induced turbulent Ekman layer. *J. Fluid Mech.* **495**, 343–368.

https://doi.org/10.1017/jfm.2013.130 Published online by Cambridge University Press